Cite this: *Dalton Trans.*, 2020, **49**, 15433

The morphology evolution, tunable down-conversion luminescence, and energy transfer of [CaY]F₂ crystals doped with Li⁺/Ce³⁺/Tb³⁺†

Yini Mao, Zhiyi Wang, Rui Ye, Li Jiang, Shanshan Hu* and Jun Yang *

Octahedral [CaY]F₂ crystals with an average particle size of 1 μm were synthesized *via* a mild one-step hydrothermal route without employing any surfactants. Various morphologies, including cubes, truncated cubes, truncated octahedrons, and spheres, were achieved *via* manipulating the amount of EDTA used, and a possible growth mechanism was proposed based on the surface energies of different crystal planes and the influence of the surfactant. XRD, SEM, EDS, TEM, HRTEM, and PL analysis were used to characterize the products. The effects of the morphologies and Li⁺ doping concentrations on the luminescence intensities of the [CaY]F₂:Ce³⁺/Tb³⁺ phosphors were explored, and the strongest luminescence intensity is obtained when the sample is cubic with (100) crystal faces and the doping concentration of Li⁺ is 0.25 mol%. Additionally, multicolor emission (blue → aquamarine blue → green) was obtained from [CaY]F₂:Ce³⁺/Tb³⁺ phosphors *via* adjusting the doping concentration of Tb³⁺, which resulted from the Ce³⁺ → Tb³⁺ energy transfer behavior; the energy transfer here happened through a dipole–dipole mechanism. This work may result in the as-synthesized phosphors having great application potential in many optoelectronic device fields, such as in displays and multicolor lighting.

Received 23rd August 2020,
Accepted 22nd October 2020
DOI: 10.1039/d0dt02955f

rsc.li/dalton

1. Introduction

Rare-earth elements have gained the reputation of being “strategic elements of the 21st century” due to their excellent physical and chemical characteristics.^{1,2} Rare-earth functional materials (with properties such as magnetism, hydrogen storage and catalytic abilities, luminescence, *etc.*) based on rare-earth elements also show unique properties, therefore, they are listed as one of the nine key materials needed for implementing a strong national manufacturing strategy.³ As a representative class of rare-earth functional materials, and as a type of inorganic material,⁴ rare-earth luminescent materials of numerous types, including oxides, fluorides, phosphates, molybdates, tungstates, aluminates, *etc.*,^{5–10} exhibit excellent optical performance, such as strong light absorption, high conversion efficiencies, pure light colors, long fluorescent lifetimes, and so on.^{11,12} So far, a variety of synthetic methods have been proposed to prepare rare-earth luminescent materials, including high-temperature solid-phase, hydrothermal, solvothermal, sol-gel, and co-precipitation

approaches.^{13–17} It must be additionally emphasized here that among these synthetic methods, hydrothermal methods are favored by researchers due to their simple operation, low energy consumption, and strong controllability, mainly in terms of morphology and size.¹⁸ The aspects mentioned above are the reasons why rare-earth luminescent materials play an indispensable role in the fields of lighting, displays, biological imaging, fluorescent labeling and medical detection.¹⁹ Furthermore, fluoride-based rare-earth luminescent materials have become the focus of most researchers due to their lower phonon energies, higher refractive indices, better chemical stabilities, larger Stokes shifts, and lower crystallization temperatures.²⁰ In the past five years, Dennis T. Klier *et al.* prepared NaYF₄:Yb,Er up-conversion nanoparticles *via* hydrothermal synthesis and characterized their temperature-dependent up-conversion luminescence with different amounts of Gd³⁺ as an additional dopant.¹⁴ M. Heise *et al.* obtained Eu³⁺-doped metal fluorides (CaF₂, SrF₂, BaF₂, and PbF₂) with fluorite structures *via* a solvent-free mechanochemical synthesis route (high-energy ball milling) and measured the luminescence lifetimes of the as-prepared nanoparticles.²⁰ Zhao and co-workers synthesized Sr₂ScF₇:Ln³⁺ (Ln = Ce, Tb, Eu, Sm, Dy, Er, Tm, Ho, and Yb) nanocrystals through a one-step hydrothermal method and studied the growth mechanism of the synthesized nanocrystals and their tunable up-/down-conversion luminescence properties, including white-light emission.²¹

School of Chemistry and Chemical Engineering, Southwest University,
No. 2 Tiansheng Road, Beibei District, Chongqing 400715, China.

E-mail: hushan3@swu.edu.cn, jyang@swu.edu.cn

†Electronic supplementary information (ESI) available. See DOI: 10.1039/d0dt02955f

It is worth noting that $[\text{CaY}]_2\text{F}_2$ is also a member of the fluoride material family, and it possesses the excellent properties of these materials, but existing research relating to it is relatively sparse, focusing only on two aspects: the improvement of synthesis methods and the up-conversion luminescence properties.^{22–24} For example, Liu and co-workers prepared rare-earth-doped $[\text{CaY}]_2\text{F}_2$ nanoparticles based on the thermal decomposition method reported by Capobianco *et al.*, and studied the up-conversion luminescence performance of $[\text{CaY}]_2\text{F}_2:\text{Yb}^{3+},\text{Er}^{3+}$ phosphors at different $\text{Yb}^{3+},\text{Er}^{3+}$ doping concentrations and the emission mechanism.²² Hu and co-workers synthesized $\text{Tm}^{3+}-\text{Yb}^{3+}$ co-doped $[\text{CaY}]_2\text{F}_2$ nanocrystals *via* utilizing a hydrothermal method, and the effects of the calcination temperature, hydrothermal reaction temperature, and rare-earth-ion doping concentration on the up-conversion luminescence properties were investigated.²³ Wang *et al.* prepared a novel photocatalyst composed of N-doped TiO_2 and $[\text{CaY}]_2\text{F}_2:\text{Yb}^{3+},\text{Tm}^{3+}$ using a combination of dealloying and a hydrothermal method.²⁴ And our group reported the synthesis, luminescence properties, and temperature-sensing capabilities of $[\text{CaY}]_2\text{F}_2:\text{Yb}^{3+},\text{Er}^{3+}$ phosphor products in a previous research work.²⁵ However, not only has no one reported on the various morphologies of $[\text{CaY}]_2\text{F}_2$ crystals and their possible evolution mechanism, but no research group has studied the intrinsic reasons for the down-conversion luminescence performance of $[\text{CaY}]_2\text{F}_2:\text{Ce}^{3+}/\text{Tb}^{3+}$ phosphors doped with Li^+ ions,^{22–26} which means that it will be a novel and challenging task to understand the crystal morphology evolution process and luminescence mechanism in detail.

In the present work, $[\text{CaY}]_2\text{F}_2$ crystals with regular octahedral shape were first synthesized *via* a mild hydrothermal method, and then the original evolution laws of crystal growth were systematically analyzed based on the surface energy of each crystal plane. Moreover, $[\text{CaY}]_2\text{F}_2$ crystals with rich morphologies, including cubes, truncated cubes, truncated octahedrons, and spheres, were synthesized *via* adding different amounts of EDTA. At the same time, the effects of EDTA on the crystal growth process were explored in detail to reveal the possible evolution mechanism of the different morphologies. In addition, the effects of the doped amount of Li^+ ions on the luminescence performance of $[\text{CaY}]_2\text{F}_2:\text{Ce}^{3+}/\text{Tb}^{3+}$ phosphors were explored on the basis of lattice defects caused by charge imbalance. Finally, the $\text{Ce}^{3+} \rightarrow \text{Tb}^{3+}$ energy transfer process and mechanism in the $[\text{CaY}]_2\text{F}_2$ host were investigated, with rich luminescent colors arising at different Tb^{3+} doping concentrations.

2. Experimental section

2.1. Chemicals

The rare earth oxides Y_2O_3 , CeO_2 , and Tb_4O_7 , with purity of 99.99%, were purchased from Ganzhou Guangli High-tech Materials Company (China). Calcium chloride (CaCl_2), lithium chloride (LiCl), sodium fluoroborate (NaBF_4), and hydrochloric acid (HCl) were obtained from Chuandong Chemical Reagents

Company (China). Ethylene diamine tetraacetic acid (EDTA) was acquired from Aladdin Industrial Corporation (China). All of the chemical reagents listed above were used directly in experiments. More particularly, rare-earth chlorides (LnCl_3) were self-prepared *via* dissolving the corresponding rare-earth oxides in hot dilute HCl and then evaporating excess HCl ; it was necessary to continuously add H_2O_2 solution during the dissolution of CeO_2 .

2.2. Synthesis

In the typical synthesis of the $[\text{CaY}]_2\text{F}_2$ host, certain proportions of CaCl_2 and YCl_3 were dissolved in 35 mL of deionized water to form a homogeneous solution upon stirring at room temperature. Afterwards, 0.7685 g of NaBF_4 was added to the mixed solution and then the mixture was fully stirred for half an hour. Finally, the obtained white suspended solution was transferred into a 50 mL stainless-steel Teflon-lined autoclave, sealed, and heated at 200 °C for 24 h. After the reaction was completed and the container was naturally cooled to room temperature, the product was collected and further purified using ethanol and deionized water several times, and then dried at 60 °C for 12 h. The preparation processes for the other products in the present work are basically the same, except the material ratios of the rare-earth elements are adjusted. If an additive was involved, it was added first, and then the other raw materials were added according to the above process after stirring for 30 minutes. It is worth noting that during Li^+ -doping, the added ratio of Y^{3+} should be reduced accordingly.

2.3. Characterization

To identify the phases of the products, X-ray diffraction (XRD) measurements were made using Purkinje General Instrument MSAL-XD3 apparatus with $\text{Cu K}\alpha$ radiation ($\lambda = 0.15406$ nm) at a scanning rate of 8°min^{-1} in the 2θ range of 10° – 90° . Morphology analysis and energy dispersive spectrometry (EDS) characterization were carried out using a field-emission scanning electron microscope (FE-SEM, Hitachi, S-4800), and transmission electron microscopy (TEM), high-resolution transmission electron microscopy (HRTEM) and selected-area electron diffraction (SAED) pattern measurements were carried out using a JEM-2100F microscope. PL excitation and emission spectra were obtained using an F-7000 spectrophotometer (Hitachi, Japan) equipped with a 150 W xenon lamp as the excitation source.

3. Results and discussion

3.1. Phases and morphologies

Fig. 1 shows the XRD pattern, the EDS spectrum, and an SEM image of pure $[\text{CaY}]_2\text{F}_2$ crystals. $[\text{CaY}]_2\text{F}_2$ was found to be cubic phase with the space group $Fm\bar{3}m$ (225) ($a = b = c = 5.5$ Å and $Z = 4$). As shown in Fig. 1a, the diffraction peaks of the sample match perfectly with the standard card (JCPDS No. 31-0293), which means that the product has high purity.²⁷ It can also be observed that the half widths of the diffraction peaks in the

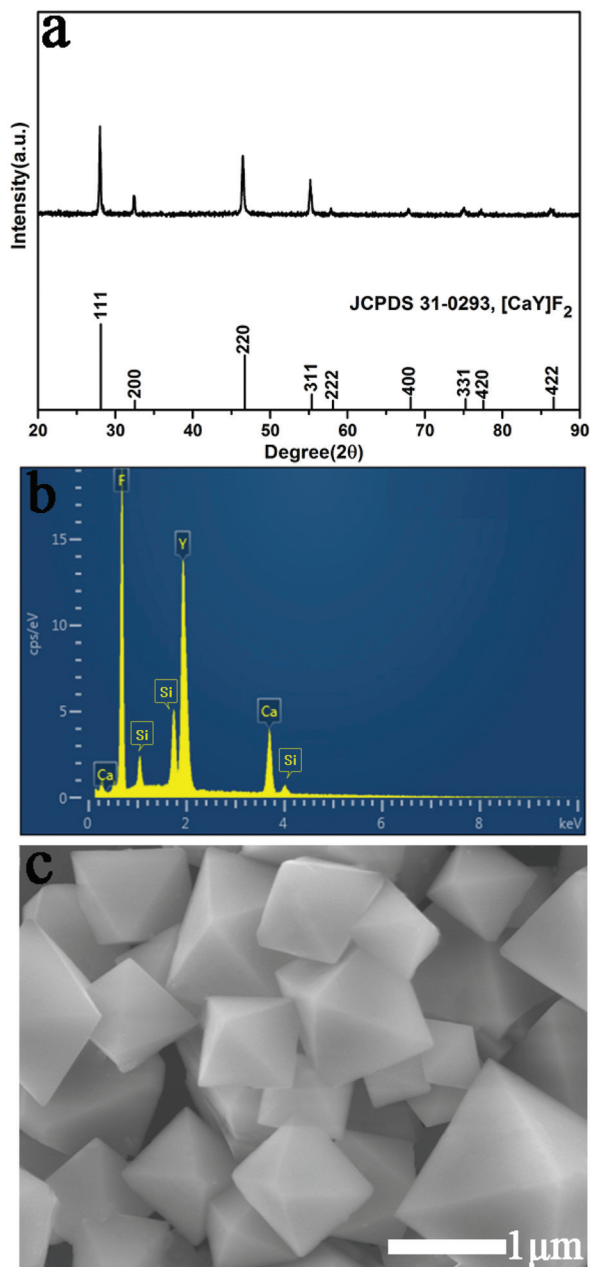


Fig. 1 Pure $[\text{CaY}]\text{F}_2$ crystals: (a) the XRD pattern, (b) the EDS spectrum, and (c) an SEM image.

XRD pattern are narrow (Fig. 1a), which reflects the high crystallinity of the prepared crystals.²⁸ Moreover, we also calculated the unit cell parameters of the sample using the measured XRD data, and the result is $a = b = c = 5.512 \text{ \AA}$; this is basically consistent with the theoretical value and can be obtained only under conditions of extremely high purity.²⁹ At the same time, Fig. 1b also provides support for the conclusion obtained from Fig. 1a that a high-purity product was synthesized. As shown in Fig. 1b, the product consists of only three elements, Ca, Y, and F, with the molar ratio of $(\text{Ca} + \text{Y}) : \text{F} = 1 : 1.98$, which is approximately equal to the theoretical value of $1 : 2$. Fig. 1c shows an SEM image of the product, in which the crystal par-

ticles are regular octahedrons with an average particle size of about $1 \mu\text{m}$. Such an appearance and size fully indicate that the product has high crystallinity.^{28,29}

To further explore the micro-morphology of the $[\text{CaY}]\text{F}_2$ crystals, TEM and HRTEM analysis was performed on the prepared products. Fig. 2a shows a TEM image of the pure $[\text{CaY}]\text{F}_2$ crystals, Fig. 2b shows a HRTEM image of a selected area (marked with a red frame in Fig. 2a), and Fig. 2c indicates images of an octahedron projected in different directions. It can be seen from Fig. 2c that an octahedron can be projected in different directions to obtain four different shapes, namely a diamond (S_1), a regular hexagon (S_2), a square (S_3), and a rectangle (S_4), which are projected in the direction of an edge, a surface, a vertex, and the direction parallel to the surface, respectively.³⁰ The above-mentioned four shapes can be observed in Fig. 2a, which proves once again that the $[\text{CaY}]\text{F}_2$ crystals appear as regular octahedron. Also, the HRTEM image

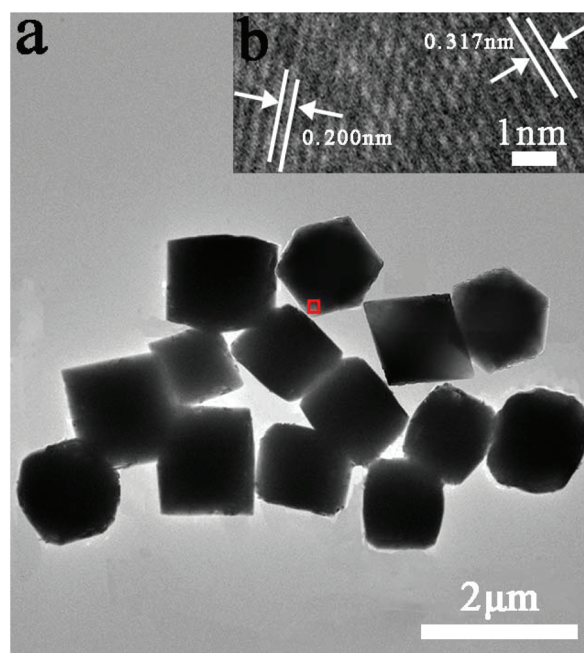


Fig. 2 (a) A TEM image of pure $[\text{CaY}]\text{F}_2$ crystals, (b) a HRTEM image from the selected area, and (c) images of an octahedron projected in different directions.

taken inside the red frame shows lattice spacings of 0.200 nm and 0.317 nm, which correspond to the interplanar spacings of the (220) and (111) crystal planes of cubic $[\text{CaY}]_2\text{F}_2$, respectively.

XRD patterns of products synthesized under different EDTA conditions are shown in Fig. 3a. The diffraction peaks of the four samples all belong to cubic $[\text{CaY}]_2\text{F}_2$ and there are no other peaks, indicating that the purities of the four samples obtained are high.²⁷ In addition, it can be found that the diffraction peaks corresponding to the (111) and (220) crystal planes are strong and sharp, reflecting that samples with high crystallinity can be obtained when the amount of EDTA added during synthesis is within a certain range.³¹

Fig. 3b–e shows SEM images of $[\text{CaY}]_2\text{F}_2$ crystals synthesized with different amounts of EDTA, and Fig. 3f shows a schematic

illustration of the morphology evolution of $[\text{CaY}]_2\text{F}_2$ crystals with varying amounts of EDTA. During the process of increasing the amount of EDTA from 0.35 g to 0.5 g, the crystals show four different morphologies, which are reflected intuitively in Fig. 3f. At the beginning, the amount of EDTA is equal to 0.35 g, and the morphology of the product is surprisingly cube shaped. More interestingly, when the amount of EDTA is changed to 0.4 g, a morphology is obtained that is formed *via* cutting off the eight corners of the cubes. Upon continuing to increase the amount of EDTA to 0.45 g, the appearance of truncated octahedrons occurs. Finally, the product is approximately uniformly spherical under the conditions of 0.5 g of EDTA. Although the appearance of the product changes as described above, the size is always on the micro-scale (Fig. 3b–e), which is completely consistent with the results obtained from the XRD patterns (Fig. 3a).

Regular octahedron crystals were obtained without using any additives (Fig. 1c), and another series of different morphologies was obtained after adding EDTA during synthesis (Fig. 3b–e). According to Gibbs–Wulff theory, the surface energy of each crystal plane is different and has the rough order of $\{hkl\} \gg \{110\} > \{100\} > \{111\}$, where $\{hkl\}$ represents the high-index crystal plane.³² The growth rates of the crystal planes also follow the above order, because the growth rate of each crystal plane is positively related to its surface energy.³³ Similarly, the final morphology of the crystal is also closely related to the above-mentioned relationship; there is such a regular pattern in the process of crystal growth that the crystal planes with faster growth rates tend to disappear, while the crystal planes with relatively slower growth rates, such as $\{110\}$, $\{100\}$, and $\{111\}$, tend to be retained.^{34,35} This is the rule explaining surface crystal plane elimination, which is why the geometric appearances of the crystals that we produced are mostly composed of $\{110\}$, $\{100\}$, and $\{111\}$ crystal planes.^{33–35}

Fig. 4a shows the evolution of the crystal shape from a cube (No. 1) to an octahedron (No. 4) due to the varying growth rates of the (100) and (111) crystal planes. For polyhedral crystals with regular shapes, the growth rate ratio $R_{(100)/(111)}$ between the (100) and (111) crystal planes is usually used to explain the evolution of crystal morphology. In our experiments, we obtained cube (0.35 g of EDTA), truncated cube (0.4 g of EDTA), truncated octahedron (0.45 g of EDTA), and regular octahedron (without EDTA) shaped crystal particles, which correspond to $R = 0.58$, $R = 0.70$, $R = 1.15$, and $R = 1.73$, respectively.³⁶ Fig. 4b shows a schematic diagram of how the (100) and (111) crystal planes change from shape 1 to shape 4. According to the direction of the arrow, the evolution process of the (100) crystal plane from existence to absence and of the (111) crystal plane from nothing to existence can be seen intuitively with the change of $R_{(100)/(111)}$.³⁶ Fig. 4c shows an illustration of the evolution of crystal growth along the (100) and (111) crystal plane directions. The law of conservation of the crystal plane angle states that the angle (dihedral angle) between any two crystal planes remains unchanged during the growth of a crystal.³⁷ As shown in Fig. 4c, the growth rate of the (100) crystal plane is faster than that of the (111) plane,

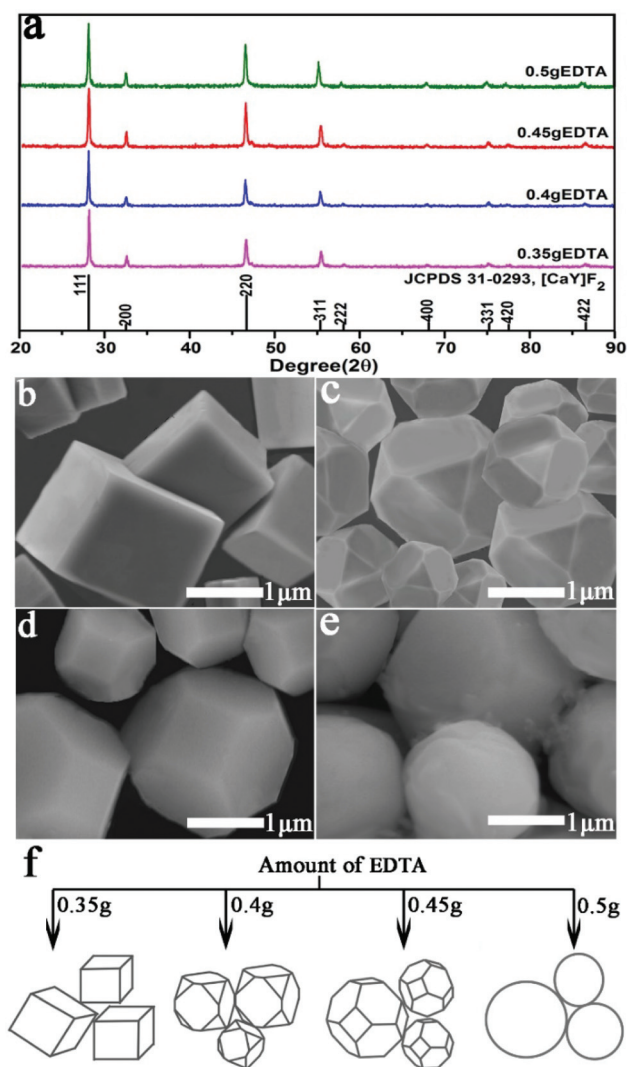


Fig. 3 XRD patterns of $[\text{CaY}]_2\text{F}_2$ crystals prepared with varying amounts of EDTA (a), SEM images of $[\text{CaY}]_2\text{F}_2$ crystals prepared with different amounts of EDTA: (b) 0.35 g, (c) 0.4 g, (d) 0.45 g, and (e) 0.5 g, and a schematic illustration of the morphology evolution of $[\text{CaY}]_2\text{F}_2$ crystals with varying amounts of EDTA (f).

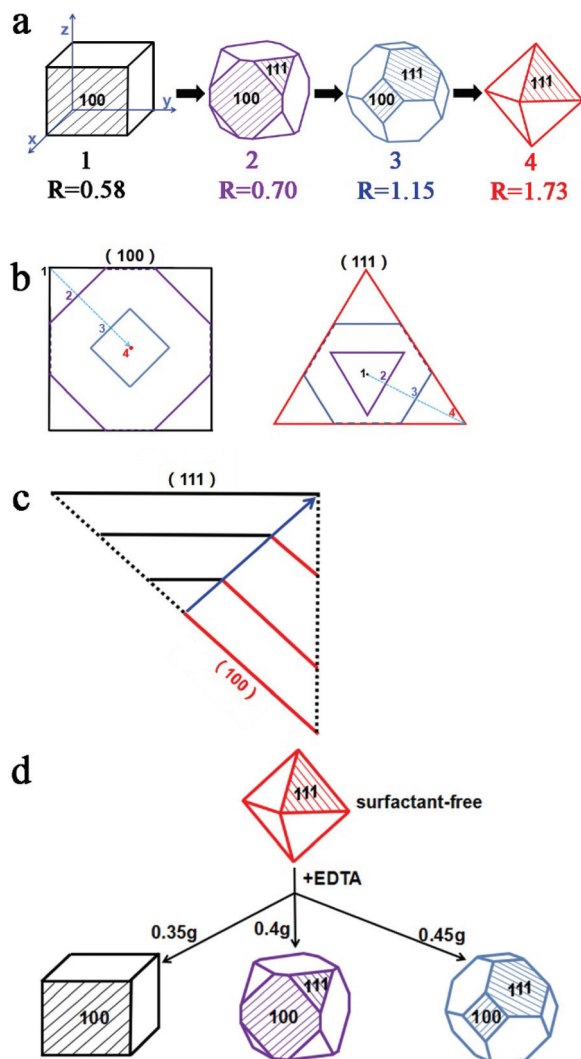


Fig. 4 (a) The evolution of the crystal shape from a cube (1) to an octahedron (4) with the varying growth rates of the (100) and (111) crystal planes, (b) a schematic diagram of the (100) and (111) crystal planes changing from shape 1 to shape 4, (c) an illustration showing the evolution of crystal growth along different directions, and (d) a schematic diagram of the effects of EDTA on crystal morphology.

and the angle between the two is a constant value. The proportion of the (100) crystal plane on the crystal surface (red) gradually decreases and finally disappears, and the proportion of the (111) plane on the crystal surface (black) gradually increases.^{37,38} This trend can be clearly seen in the direction of the arrow, which again points out that the final morphology of the crystal depends on the relative growth rates of the crystal planes, and the proportion of the crystal plane with a slower growth rate on the surface of the crystal product is relatively large.³³

However, it is worth noting that we did not directly obtain the crystal morphology evolution pattern seen in Fig. 4a during the preparation process, but instead obtained a variety of products with different morphologies in the order seen in Fig. 4d, which is due to the influence of the surfactant.³⁹ During the process of crystal growth, the addition of some

kinds of surfactants will cause preferential adsorption effects on some crystal planes, resulting in a change in the order of surface energies (growth rates).^{40,41} Here, the existence of EDTA swapped the surface energy order of the (111) and (100) crystal planes. When EDTA is absent, the composition of the crystal surface is dominated by the (111) crystal plane with the slowest growth rate, and there is no (100) crystal plane (Fig. 4d). After adding EDTA during the synthesis process, it will selectively adsorb on the (100) crystal plane of the $[\text{CaY}]\text{F}_2$ crystals *via* electrostatic interactions, making the binding energy of the (100) crystal plane smaller and correspondingly reducing the growth rate.^{41,42} This will result in the exposure of the (100) surface, and will contribute to the generation of the final geometric appearance of the crystal.³⁵ The proportion changed depending on the amount of EDTA added (Fig. 4d). When the amount of EDTA is equal to 0.35 g, the (100) crystal plane is the main one (Fig. 4d). Then, the proportion of the (100) crystal plane gradually decreases as the amount of EDTA increases (Fig. 4d). Therefore, a product with desired morphology can be obtained *via* adding an appropriate amount of surfactant during the synthesis of the crystals.⁴³

3.2. Down-conversion luminescence

3.2.1. Morphology-dependent luminescence properties.

Based on the morphologies of the samples, $[\text{CaY}]\text{F}_2:0.1\%\text{Tb}^{3+}$ phosphors synthesized with 0 g of EDTA (octahedrons), 0.35 g of EDTA (cubes), 0.4 g of EDTA (truncated cubes), 0.45 g of EDTA (truncated octahedrons), and 0.5 g of EDTA (spheres) were used as examples to explore the effects of morphology on luminescence properties.

Fig. 5 shows the emission spectra of $[\text{CaY}]\text{F}_2:0.1\%\text{Tb}^{3+}$ phosphors synthesized with different EDTA content levels, and an illustration showing the corresponding morphology of each sample. The morphologies of the products are almost the same as those without Tb^{3+} doping, which indicates that doping a relatively small amount of rare-earth ions will not

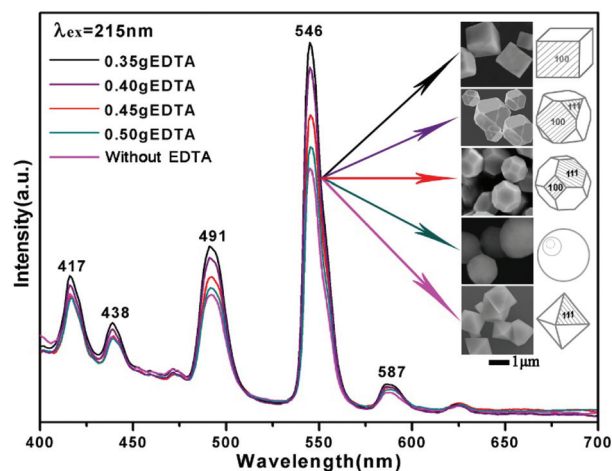


Fig. 5 The emission spectra of $[\text{CaY}]\text{F}_2:0.1\%\text{Tb}^{3+}$ phosphors synthesized with different EDTA content levels; the corresponding morphologies of the samples are shown in the illustration.

cause changes in the morphologies of the products.⁴⁴ In addition, Y^{3+} and Tb^{3+} belong to the heavy rare-earth group, which is also an auxiliary factor in the maintenance of morphology.⁴⁵ It can be seen from Fig. 5 that the cube-shaped sample whose surface structure is dominated by the (100) crystal plane has the largest luminescence intensity, and then the luminescence intensity gradually decreases with a decrease in the proportion of the (100) crystal plane on each crystal surface, indicating that the doped rare-earth light-emitting ions (Tb^{3+}) were mainly concentrated on the (100) crystal plane.⁴⁶ In other words, changes in the morphologies (the proportions of crystal planes) of the samples caused by EDTA are the root cause of the different luminescence intensities of each sample.

In order to further prove the above conclusions that Tb^{3+} was mainly doped into the (100) crystal plane, the interplanar spacing values before and after doping are calculated and shown in Table 1. We know that the doping of rare-earth ions into the crystal lattice of the host will cause changes in the interplanar spacing²¹ (here, the change in the interplanar spacing after doping is represented by Δd), which can reflect the ion-doping situation to a certain extent. The larger the Δd value, the greater the possibility of doping into the corresponding crystal plane.⁴⁶ According to the variation of Δd , it can be seen that Tb^{3+} ions are indeed doped mainly into the (200) crystal plane of $[CaY]F_2$, which is also the (100) crystal plane. Therefore, the results in Table 1 provide reasonable support for the conclusions made from Fig. 5. For further proof, we analyzed the quantum yields of samples with different morphologies (Tables S1 and S2 in the ESI[†]), and the results obtained are consistent with the experimental results shown in Fig. 5.

3.2.2. Influence of the Li^+ -doping concentration. In $[CaY]F_2$, Ca^{2+} and Y^{3+} ions actually occupy the same lattice sites, with the same structure as CaF_2 ; however, Y^{3+} occupying Ca^{2+} lattice sites will cause an imbalance of positive and negative charges, which will then cause lattice defects.⁴⁷ Lattice defects usually act as luminescence quenchers, and positive monovalent alkali metal cations are often required to act as charge compensators in this case.⁴⁷ Li^+ not only has similar electronegativity as Y^{3+} , but it also has a radius that is not much different from Y^{3+} , so charge compensation can be carried out through doping with Li^+ ions.⁴⁸ As shown in Fig. 6a, cation vacancies are introduced in order to maintain charge balance in the case without Li^+ -ion doping, and charge compensation can be performed after doping with Li^+ ions (Fig. 6b).^{47,48}

Based on the above analysis, the effects of the Li^+ -doping concentration on down-conversion luminescence were

Table 1 $[CaY]F_2:0.1\%Tb^{3+}$ interplanar spacing of the four main crystal planes

	(111)	(200)	(220)	(311)
$[CaY]F_2$	3.170	2.751	1.943	1.658
$[CaY]F_2:0.1\%Tb^{3+}$	3.169	2.744	1.941	1.657
Δd	0.001	0.007	0.002	0.001

explored. Fig. 7 shows the emission spectra of $[CaY]F_2:10\%Ce^{3+}$ (Fig. 7a) and $[CaY]F_2:0.7\%Tb^{3+}$ (Fig. 7b) phosphors as a function of Li^+ -doping concentration, and the insets show charts of emission peak intensity as a function of Li^+ -doping concentration. It can be seen that the luminescence intensity of the phosphor is greatly affected by the Li^+ -doping concentration. As the doping concentration of Li^+ increases, the luminescence intensity first increases and then decreases, and it is surprising to find that the luminescence intensities of the two phosphors both reach maximum values when the Li^+ -doping concentration is 0.25 mmol, that is, when Li^+ replaces just half of the total amount (0.50 mmol) of Ln^{3+} ($Ln = Y, Ce, Tb$). This can be reasonably explained using Fig. 6c. In theory, when Li^+ ions and $Y^{3+}/Ce^{3+}/Tb^{3+}$ ions enter Ca^{2+} lattice sites at a ratio of 1 : 1, the charge will be completely balanced to minimize lattice defects.⁴⁹ And, naturally, the luminescence intensity at this time is the largest. Too much or too little Li^+ -ion doping will reduce the luminescence intensity due to corresponding lattice defects (Fig. 6a and d), so the luminescence intensity shows a quadratic function trend of rising and then falling (the insets of Fig. 7).⁴⁹

3.3. Energy transfer behavior

Fig. 8 shows the excitation and emission spectra of $[CaY]F_2:10\%Ce^{3+}$, $[CaY]F_2:0.7\%Tb^{3+}$, and $[CaY]F_2:10\%Ce^{3+},0.7\%Tb^{3+}$ phosphors. It can be seen from Fig. 8a that the emission spec-

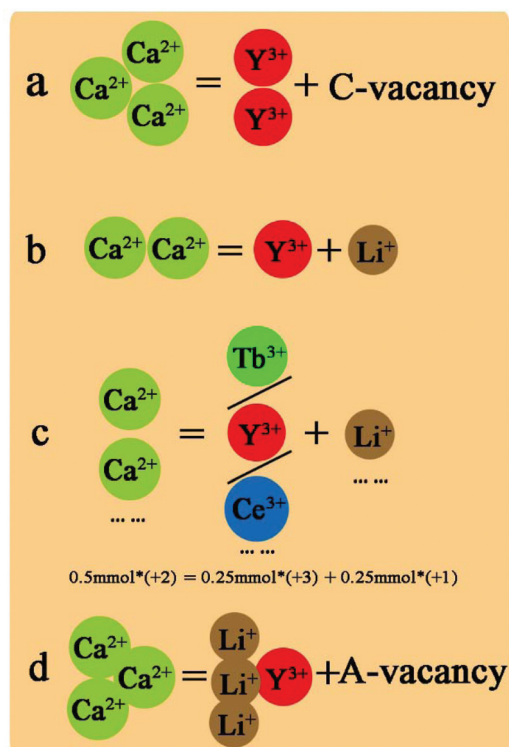


Fig. 6 A schematic representation of charge compensation without Li^+ (a) and with Li^+ co-doping in $[CaY]F_2$ (b), and with Li^+ co-doping in $[CaY]F_2:Ce^{3+}/Tb^{3+}$ phosphors (c), and a schematic diagram of the introduction of A-vacancies (d).

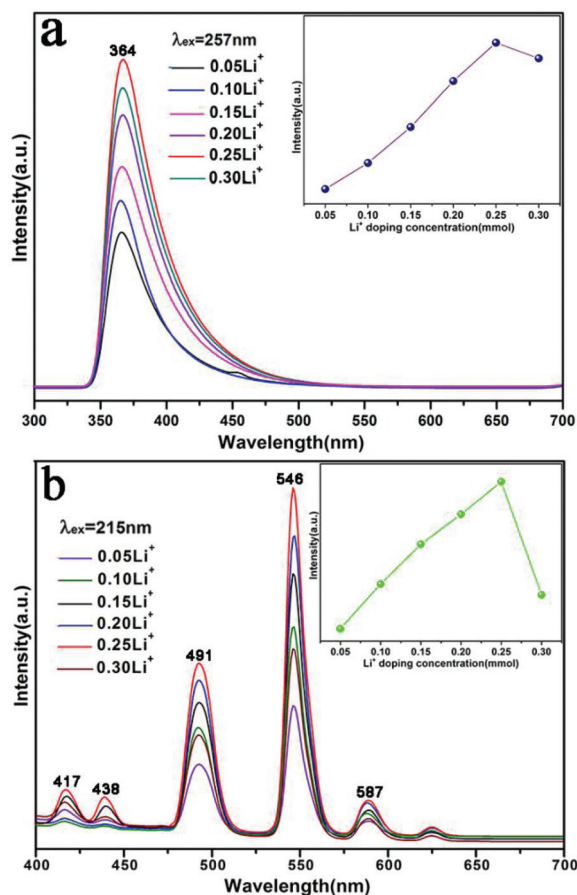


Fig. 7 Emission spectra of $[\text{CaY}]_2\text{F}_2:10\%\text{Ce}^{3+}$ (a) and $[\text{CaY}]_2\text{F}_2:0.7\%\text{Tb}^{3+}$ (b) phosphors as a function of Li^+ doping concentration; the insets show charts of emission peak intensity as a function of Li^+ -doping concentration.

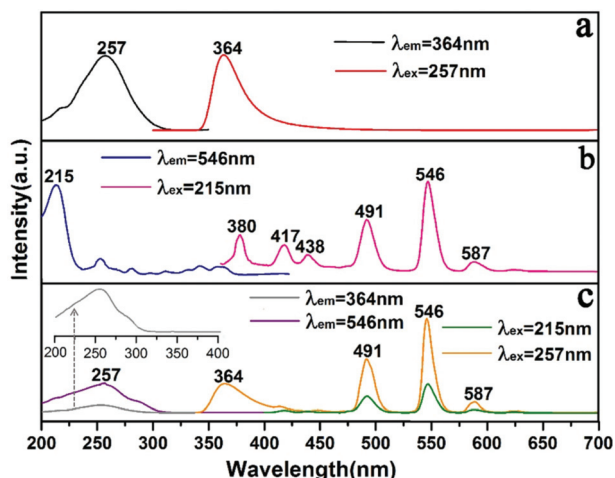


Fig. 8 The excitation and emission spectra of $[\text{CaY}]_2\text{F}_2:10\%\text{Ce}^{3+}$ (a), $[\text{CaY}]_2\text{F}_2:0.7\%\text{Tb}^{3+}$ (b), and $[\text{CaY}]_2\text{F}_2:10\%\text{Ce}^{3+},0.7\%\text{Tb}^{3+}$ (c), respectively.

trum of Ce^{3+} consists of a broad and strong peak at 364 nm when 257 nm was used as the excitation wavelength, which is derived from a Ce^{3+} transition from 5d to 4f. At the monitoring

wavelength of 364 nm, the excitation spectrum is also composed of a broad peak, which is generated during the transition of electrons from the ground state ($^2\text{F}_{5/2}$) to the excited state (5d).⁵⁰ As shown in Fig. 8b, upon excitation at 215 nm, the emission spectrum of $[\text{CaY}]_2\text{F}_2:0.7\%\text{Tb}^{3+}$ is composed of multiple emission peaks in the range of 380–600 nm, with a maximum at 546 nm ($^5\text{D}_4 \rightarrow ^7\text{F}_5$). The remaining emission peaks are located at 380 nm ($^5\text{D}_3 \rightarrow ^7\text{F}_6$), 417 nm ($^5\text{D}_3 \rightarrow ^7\text{F}_5$), 438 nm ($^5\text{D}_3 \rightarrow ^7\text{F}_4$), 491 nm ($^5\text{D}_4 \rightarrow ^7\text{F}_6$), 546 nm ($^5\text{D}_4 \rightarrow ^7\text{F}_5$), and 587 nm ($^5\text{D}_4 \rightarrow ^7\text{F}_4$). At a monitoring wavelength of 546 nm, it is observed that the excitation spectrum mainly consists of a strong excitation peak at 215 nm and some weak peaks in the range of 230–380 nm, which are attributed to a $4\text{f}^8-4\text{f}^75\text{d}^1$ spin-allowed transition ($^7\text{F}_6 \rightarrow ^7\text{D}_J$) and spin-forbidden transition ($^7\text{F}_6 \rightarrow ^9\text{D}_J$), respectively, in Tb^{3+} .^{51,52}

By comparing Fig. 8(a) and (b), it can be found that the emission spectrum of Ce^{3+} overlaps with the excitation spectrum of Tb^{3+} to a certain extent, from which it can be preliminarily inferred that $\text{Ce}^{3+} \rightarrow \text{Tb}^{3+}$ energy transfer may occur in the $[\text{CaY}]_2\text{F}_2$ host.⁵³ It can be seen from Fig. 8c that not only the emission peak from Ce^{3+} but also the emission peak from Tb^{3+} are obtained at an excitation wavelength of 257 nm, revealing that the Tb^{3+} ions are essentially excited through the Ce^{3+} ions. More importantly, the emission peak from Tb^{3+} obtained under these conditions is much stronger than that obtained under excitation at 215 nm, which indicates that energy has been successfully transferred from Ce^{3+} to Tb^{3+} .⁵³ It can also be seen from Fig. 8c that the excitation spectrum of $[\text{CaY}]_2\text{F}_2:10\%\text{Ce}^{3+},0.7\%\text{Tb}^{3+}$ monitored at 546 nm (Tb^{3+} emission) is similar to that monitored at 364 nm (Ce^{3+} emission), with differences only in relative intensity; also, the excitation spectrum of $[\text{CaY}]_2\text{F}_2:10\%\text{Ce}^{3+},0.7\%\text{Tb}^{3+}$ monitored at 364 nm (Ce^{3+} emission) seen in Fig. 8c is the same as the excitation spectrum of $[\text{CaY}]_2\text{F}_2:10\%\text{Ce}^{3+}$ monitored at 364 nm (Ce^{3+} emission) in Fig. 8a, and there is no characteristic excitation peak from Tb^{3+} ions, which proves that there is no energy migration from the 4f-5d excited state of Tb^{3+} to the 4f-5d excited state of Ce^{3+} . Since then, we explored the luminescence properties of a series of Ce^{3+} and Tb^{3+} co-doped phosphors. Fig. 9a shows the emission spectra of $[\text{CaY}]_2\text{F}_2:10\%\text{Ce}^{3+},x\%\text{Tb}^{3+}$ ($x = 0, 0.3, 0.5, 0.7, 0.9, 1.3, \text{ and } 1.5$) phosphors. The doping concentration of Ce^{3+} is fixed at 10%. With an increase in Tb^{3+} , the intensity of the characteristic peak at 546 nm (Tb^{3+} , $^5\text{D}_4 \rightarrow ^7\text{F}_5$) gradually increases and reaches a maximum at $x = 0.7$, then gradually weakens due to concentration quenching effects.⁵⁴ Correspondingly, the intensity of the characteristic peak at 364 nm (Ce^{3+} , $5\text{d} \rightarrow 4\text{f}$) continued to decrease due to the occurrence of $\text{Ce}^{3+} \rightarrow \text{Tb}^{3+}$ energy transfer.⁵⁵ Fig. 9b shows the CIE chromaticity coordinates of the phosphors mentioned above. When the Tb^{3+} concentration was changed from 0% to 1.5%, the chromaticity coordinates methodically changed from blue (0.1589, 0.0496) to aquamarine blue (0.2268, 0.3349), and finally to green (0.2516, 0.5126), which indicates that the regulation of luminescent color can be achieved during the energy transfer process.

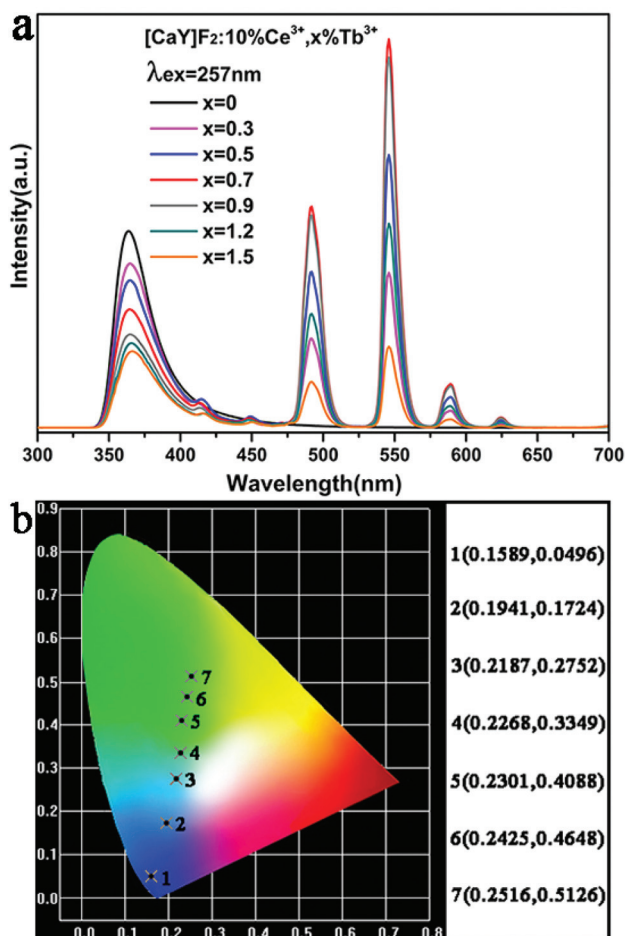


Fig. 9 (a) A series of emission spectra from $[\text{CaY}]\text{F}_2:10\%\text{Ce}^{3+},x\%\text{Tb}^{3+}$ and (b) the corresponding CIE chromaticity coordinates of $[\text{CaY}]\text{F}_2:10\%\text{Ce}^{3+},x\%\text{Tb}^{3+}$ phosphors ($x = 0, 0.3, 0.5, 0.7, 0.9, 1.3,$ and 1.5).

For a deeper understanding of the process of $\text{Ce}^{3+} \rightarrow \text{Tb}^{3+}$ energy transfer, we calculated the energy transfer efficiencies of $[\text{CaY}]\text{F}_2:10\%\text{Ce}^{3+},x\%\text{Tb}^{3+}$ ($x = 0, 0.3, 0.5, 0.7, 0.9, 1.3,$ and 1.5) phosphors *via* the following formula:⁵⁶

$$\eta_{\text{T}} = 1 - \frac{I_{\text{S}}}{I_{\text{S}_0}}$$

where I_{S} and I_{S_0} in the formula indicate the emission intensity of Ce^{3+} in the presence and absence of Tb^{3+} , respectively, and η_{T} is the energy transfer efficiency. According to the calculation results, it can be concluded that the energy transfer efficiency can reach 87.1% in the experimental range. Fig. 10 reveals the relative emission intensity trends of Ce^{3+} (364 nm) and Tb^{3+} (546 nm), and the energy transfer efficiency change with the Tb^{3+} concentration, which can more intuitively reflect the conclusions obtained in Fig. 9a. Before the emission of Tb^{3+} at 546 nm reached its strongest value, the energy transfer efficiency increased rapidly from 0% to 60.2%, and then the growth rate gradually decreased, and the efficiency slowly reached 87.1%. The luminescence decay curves of Ce^{3+} emission from $[\text{CaY}]\text{F}_2:10\%\text{Ce}^{3+},x\%\text{Tb}^{3+}$ ($x = 0, 0.3, 0.5, 0.7, 0.9,$

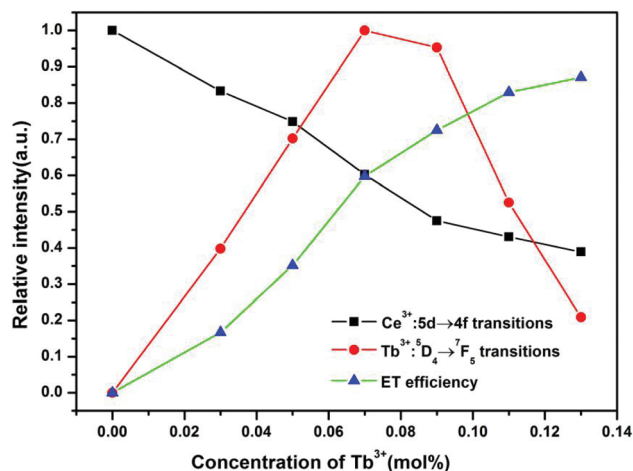


Fig. 10 The relative emission intensities of Ce^{3+} at 364 nm and Tb^{3+} at 546 nm, and the ET efficiency of $\text{Ce}^{3+} \rightarrow \text{Tb}^{3+}$ in $[\text{CaY}]\text{F}_2:10\%\text{Ce}^{3+},x\%\text{Tb}^{3+}$ phosphors.

1.2, and 1.5) were measured to further understand the excited state dynamics of the energy transfer process (Fig. S1†). The decay time of Ce^{3+} decreases monotonically with an increase in Tb^{3+} concentration, which proves that efficient energy transfer from Ce^{3+} to Tb^{3+} occurred.

Then, the $\text{Ce}^{3+} \rightarrow \text{Tb}^{3+}$ ET mechanism was explored. According to the literature, the ET mechanism is closely related to the critical distance (R_{C}) between the sensitizer and activator ions. When $R_{\text{C}} \geq 4 \text{ \AA}$, ET mainly occurs through electric multipolar interactions, and when $R_{\text{C}} < 4 \text{ \AA}$, exchange interactions are taken to be dominant.⁵⁷ The following formula can be used to calculate the critical distance R_{C} :⁵⁷

$$R_{\text{C}} \approx 2 \left[\frac{3V}{4\pi\chi_{\text{c}}N} \right]^{1/3}$$

where π is a constant, χ_{c} represents the total concentration of Ce^{3+} and Tb^{3+} when the luminescence intensity of Ce^{3+} is half that in the absence of Tb^{3+} (it is estimated that the concentrations of Ce^{3+} and Tb^{3+} here are 10% and 0.7%, respectively), V represents the volume of the unit cell, and N is the number of molecules in a unit cell. For $[\text{CaY}]\text{F}_2$, substituting $V = 166.4$, $N = 4$, and $\chi_{\text{c}} = 0.107$ into the formula results in $R_{\text{C}} = 9.06 \text{ \AA}$, which is $>4 \text{ \AA}$, so $\text{Ce}^{3+} \rightarrow \text{Tb}^{3+}$ energy transfer here occurs mainly through electric multipolar interactions. Electric multipolar interactions can be further divided into three types: dipole–dipole (D–D), dipole–quadrupole (D–Q), and quadrupole–quadrupole (Q–Q) interaction.⁵⁸ The following relationship can be used to make an accurate judgment:⁵⁹

$$\frac{\eta_{\text{S}_0}}{\eta_{\text{S}}} \propto C^n$$

where $\eta_{\text{S}_0}/\eta_{\text{S}}$ can be approximated by $I_{\text{S}_0}/I_{\text{S}}$, which is the ratio of the Ce^{3+} emission intensity in the absence and presence of Tb^{3+} , C represents the total concentration of Ce^{3+} and Tb^{3+} ions, and $n = 6, 8, 10$ correspond to the above-mentioned D–D, D–Q, and Q–Q interactions, respectively. The linear relation-

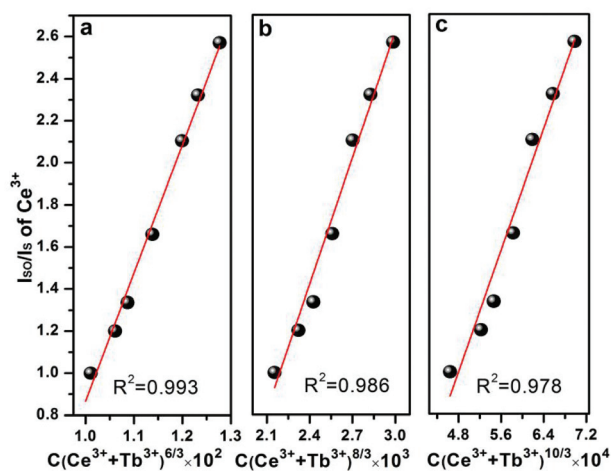


Fig. 11 The dependence of $Ce^{3+} I_{S0}/I_S$ on (a) $C(Ce^{3+} + Tb^{3+})^{6/3}$, (b) $C(Ce^{3+} + Tb^{3+})^{8/3}$, and (c) $C(Ce^{3+} + Tb^{3+})^{10/3}$.

ships between I_{S0}/I_S and $(Ce^{3+} + Tb^{3+})^{n/3}$ are shown in Fig. 11; it can be seen that R^2 has a maximum value of 0.993 when $n = 6$, which indicates that the $Ce^{3+} \rightarrow Tb^{3+}$ energy transfer here mainly occurs through a dipole–dipole interaction mechanism.

4. Conclusions

To sum up, cubic phase octahedral $[CaY]F_2$ crystals were successfully synthesized *via* a mild one-step hydrothermal route without employing any surfactants. Also, $[CaY]F_2$ crystals with different microscale morphologies (cubes, truncated cubes, truncated octahedrons, and spheres) were prepared *via* varying the amount of EDTA used. The formation mechanisms for the various morphologies are related to the surface energy of each crystal plane; the presence of a surfactant will disrupt the original regularity of crystal growth, originating from the preferential adsorption of the surfactant on certain crystal planes, which causes the surface energies (growth rates) of the crystal planes to change sequentially. The luminescence intensity of the $[CaY]F_2:Tb^{3+}$ phosphors reached a maximum when the microscopic appearance was cubic, because Tb^{3+} ions are mainly doped on the (110) crystal plane, which accounts for the largest proportion of the cubic morphology. Also, the $[CaY]F_2:Ln^{3+}$ ($Ln = Ce, Tb$) phosphors exhibit the strongest emission when the Li^+ -doping concentration is 0.25 mmol, because the charges are completely balanced at this time and lattice defects are correspondingly reduced to a minimum. The $Ce^{3+} \rightarrow Tb^{3+}$ ET processes were dominated by dipole–dipole interactions. The $[CaY]F_2:Ce^{3+}, Tb^{3+}$ phosphors showed richer emission colors due to efficient ET from Ce^{3+} to Tb^{3+} ; as the Tb^{3+} doping amount increased, the emission color could be tuned from blue to aquamarine and then to green. The convenient synthesis route and effective tunable emission might promote the development and application of the prepared phosphors in optoelectronic-device fields.

Conflicts of interest

There are no conflicts of interest to declare.

Acknowledgements

This project is financially sponsored by the Natural Science Foundation of Chongqing, China (cstc2020jcyj-msxmX0332).

Notes and references

- J. M. Klinger, *Extr. Ind. Soc.*, 2015, **2**(3), 572–580.
- G. Lin, L. Zhang, S. Yin, J. Peng, S. Li and F. Xie, *Green Process. Synth.*, 2015, **4**(4), 329–336.
- S. V. Eliseeva and J. C. Bünzli, *Chem. Soc. Rev.*, 2010, **39**(1), 189–227.
- S. V. Eliseeva and J. C. G. Bünzli, *New J. Chem.*, 2011, **35**(6), 1165.
- F. Sordello, I. Berruti, C. Gionco, M. C. Paganini, P. Calza and C. Minero, *Appl. Catal., B*, 2019, **245**, 159–166.
- M. Tan, B. del Rosal, Y. Zhang, E. Martín Rodríguez, J. Hu, Z. Zhou, R. Fan, D. H. Ortgies, N. Fernández, I. Chaves-Coira, Á. Núñez, D. Jaque and G. Chen, *Nanoscale*, 2018, **10**(37), 17771–17780.
- H. Guo, X. Huang and Y. Zeng, *J. Alloys Compd.*, 2018, **741**, 300–306.
- Y. Wu, H. Suo, D. He and C. Guo, *Mater. Res. Bull.*, 2018, **106**, 14–18.
- Z. Zou, T. Wu, H. Lu, Y. Tu, S. Zhao, S. Xie, F. Han and S. Xu, *RSC Adv.*, 2018, **8**(14), 7679–7686.
- G. Zhang, Q. Qiang, S. Du and Y. Wang, *RSC Adv.*, 2018, **8**(17), 9512–9518.
- Z. K. Zhang, M. L. Bai, D. Z. Guo, S. M. Hou and G. M. Zhang, *Chem. Commun.*, 2011, **47**(29), 8439.
- F. Qi, F. Huang, L. Zhou, Y. Tian, R. Lei, G. Ren, J. Zhang, L. Zhang and S. Xu, *J. Alloys Compd.*, 2018, **731**, 418–422.
- K. Upadhyay, R. K. Tamrakar and V. Dubey, *Superlattices Microstruct.*, 2015, **78**, 116–124.
- D. T. Klier and M. U. Kumke, *J. Phys. Chem. C*, 2015, **119**(6), 3363–3373.
- N. Panov, R. Marin and E. Hemmer, *Inorg. Chem.*, 2018, **57**(23), 14920–14929.
- M. N. Akhtar and M. A. Khan, *J. Magn. Magn. Mater.*, 2018, **460**, 268–277.
- A. Manikandan, E. Manikandan, B. Meenatchi, S. Vadivel, S. K. Jaganathan, R. Ladchumananandasivam, M. Henini, M. Maaza and J. S. Aanand, *J. Alloys Compd.*, 2017, **723**, 1155–1161.
- Y. Luo, R. Yang, X. Zhang, B. Hu, S. Hu, L. Zhou and J. Yang, *CrystEngComm*, 2015, **17**(40), 7762–7771.
- A. Escudero, C. Carrillo-Carrion, M. V. Zyuzin and W. J. Parak, *Top. Curr. Chem.*, 2016, **374**(4), 48.
- M. Heise, G. Scholz, T. Krahl and E. Kemnitz, *Solid State Sci.*, 2019, **91**, 113–118.

- 21 B. Zhao, D. Shen, J. Yang, S. Hu, X. Zhou and J. Tang, *J. Mater. Chem. C*, 2017, **5**(13), 3264–3275.
- 22 Y. C. Liu, *J. Inner Mongolia Normal Univ. (Nat. Sci. Edit.)*, 2015, **44**(4), 481–487.
- 23 W. Hu, X. Hu, H. Wang, X. Zhao, D. Xia, C. Feng, C. Liang, Y. Dong, X. Cheng and Q. Li, *J. Mater. Sci.: Mater. Electron.*, 2017, **28**(16), 12290–12296.
- 24 L. Wang, C. Xia, T. Yang, H. Wang, N. Liu and C. Liang, *Nanotechnology*, 2020, **31**(2), 025601.
- 25 Y. L. Liu, Y. N. Mao and J. Yang, *J. Liaocheng Univ. (Nat. Sci.)*, 2020, **33**(4), 39–44.
- 26 W. Li, H. Huang, B. Mei, J. Song and X. Xu, *J. Alloys Compd.*, 2018, **747**, 359–365.
- 27 X. F. Wu, G. S. Hu, B. B. Wang and Y. F. Yang, *J. Cryst. Growth*, 2008, **310**(2), 457–461.
- 28 M. Bellardita, A. Di Paola, B. Megna and L. Palmisano, *Appl. Catal., B*, 2017, **201**, 150–158.
- 29 L. Zhou, S. Hu, X. Zhou, J. Tang and J. Yang, *CrystEngComm*, 2016, **18**(39), 7590–7600.
- 30 M. A. Ramos-Docampo, B. Rivas-Murias, B. Rodríguez-González and V. Salgueiriño, *CrystEngComm*, 2017, **19**(37), 5542–5548.
- 31 Y. Zeng, Z. Lin, Y. Meng, Y. Wang, M. Yu, X. Lu and Y. Tong, *Adv. Mater.*, 2016, **28**(41), 9188–9195.
- 32 T. Li, M. He and W. Zeng, *J. Alloys Compd.*, 2017, **712**, 50–58.
- 33 S. Sun, X. Zhang, Q. Yang, S. Liang, X. Zhang and Z. Yang, *Prog. Mater. Sci.*, 2018, **96**, 111–173.
- 34 Z. Y. Zhou, N. Tian, J. T. Li, I. Broadwell and S. G. Sun, *Chem. Soc. Rev.*, 2011, **40**(7), 4167–4185.
- 35 Y. J. Wang, W. Long, L. Wang, R. Yuan, A. Ignaszak, B. Fang and D. P. Wilkinson, *Energy Environ. Sci.*, 2018, **11**(2), 258–275.
- 36 H. Zheng, Q. Li, C. Yang, H. Lin, M. Nie, L. Qin and Y. Li, *RSC Adv.*, 2015, **5**(73), 59349–59353.
- 37 S. Sun, H. Zhang, X. Song, S. Liang, C. Kong and Z. Yang, *CrystEngComm*, 2011, **13**(20), 6040.
- 38 P. Y. Cao, Y. L. Liu, Z. T. Lin, J. F. Huang, W. Z. Chen, J. H. Liang, W. Zhou and G. B. Jiang, *Carbon*, 2017, **118**, 625–633.
- 39 Y. Yin and A. P. Alivisatos, *Nature*, 2005, **437**(7059), 664–670.
- 40 D. L. Liao and B. Q. Liao, *J. Photochem. Photobiol., A*, 2007, **187**(2–3), 363–369.
- 41 D. F. Zhang, H. Zhang, L. Guo, K. Zheng, X. D. Han and Z. Zhang, *J. Mater. Chem.*, 2009, **19**(29), 5220.
- 42 W. J. Ong, L. L. Tan, S. P. Chai, S. T. Yong and A. R. Mohamed, *Nanoscale*, 2014, **6**(4), 1946–2008.
- 43 X. Pan, M. Q. Yang and Y. J. Xu, *Phys. Chem. Chem. Phys.*, 2014, **16**(12), 5589.
- 44 Y. Zhai, Q. Sun, S. Yang, X. Zhao, T. Li and H. Wang, *Optik*, 2018, **174**, 600–608.
- 45 J. Cao, L. Yuan, S. Hu, J. Tang, X. Zhou and J. Yang, *CrystEngComm*, 2016, **18**(31), 5940–5951.
- 46 Y. Y. Ma, *Bohai Univ.*, 2018, 51–55.
- 47 D. Jiaren, Q. D. C. Olivier, K. Katleen and P. Dirk, *Materials*, 2017, **10**(12), 1422.
- 48 D. Prakashbabu, H. B. Ramalingam, R. Hari Krishna, B. M. Nagabhushana, R. Chandramohan, C. Shivakumara, J. Thirumalai and T. Thomas, *Phys. Chem. Chem. Phys.*, 2016, **18**(42), 29447–29457.
- 49 Y. Tan, Y. Yan, H. Du, X. Hu, G. Li, Y. Kuang, M. Li and D. Guo, *Opt. Mater.*, 2018, **85**, 538–544.
- 50 M. Ding, H. Zhang, D. Chen, J. Xi, Q. Hu and Z. Ji, *J. Alloys Compd.*, 2016, **672**, 117–124.
- 51 Y. N. Mao and S. S. Hu, *J. Liaocheng Univ. (Nat. Sci.)*, 2020, **33**(3), 51–56.
- 52 S. Lun, E. Liu, J. Fan, X. Hu, J. Wan, J. Li, H. Li and Y. Hu, *J. Lumin.*, 2015, **166**, 361–365.
- 53 M. Y. A. Yagoub, H. C. Swart and E. Coetsee, *J. Lumin.*, 2017, **187**, 96–101.
- 54 S. Xu, Z. Wang, P. Li, T. Li, Q. Bai, J. Sun and Z. Yang, *J. Am. Ceram. Soc.*, 2017, **100**(5), 2069–2080.
- 55 X. Wu, Y. Jiao, O. Hai, Q. Ren, F. Lin and H. Li, *J. Alloys Compd.*, 2018, **730**, 521–527.
- 56 Q. Bao, Z. Wang, Q. Feng, Z. Wang, X. Meng, K. Qiu, Y. Chen, J. Sun, Z. Yang and P. Li, *J. Lumin.*, 2019, **213**, 164–173.
- 57 Y. Tian, Y. Wei, Y. Zhao, Z. Quan, G. Li and J. Lin, *J. Mater. Chem. C*, 2016, **4**(6), 1281–1294.
- 58 J. Huo, W. Lü, B. Shao, Y. Feng, S. Zhao and H. You, *Dyes Pigm.*, 2017, **139**, 174–179.
- 59 X. Mi, J. Sun, P. Zhou, H. Zhou, D. Song, K. Li, M. Shang and J. Lin, *J. Mater. Chem. C*, 2015, **3**(17), 4471–4481.